Flow field investigation of Confined Coaxial Swirling Jets by Stereo-PIV

Flow field investigation of Confined Coaxial Swirling Jets by Stereo-PIV

F. Cozzi[1], A. Francabandiera[1], L. Zampini[2]

[1] Politecnico Milano, Dipartimento di Energia, Via Lambruschini 4, Milano, Italy
[2] Turbomachinery and propulsion department Von Karman Institute for Fluid Dynamics, Rhode Saint Genese, Bruxelles 95616, Belgium

Email: fabio.cozzi@polimi.it

ORCID ID: 0000-0003-1350-2627

Abstract. This work analyses the isothermal flow field of a research burner exploiting both swirl and radially staged combustion air. The burner is composed of two coaxial co-rotating swirling jets, and the swirl level of the two jets can be controlled independently of each other. The influence of the swirl levels on the flow field is experimentally investigated under isothermal conditions using the Stereo-PIV technique, and the results evidence significant differences in the mean flow field at the different swirl levels. The vortex breakdown occurs in all the investigated cases, except for the combination of the lowest outer swirl level and the intermediate inner swirl level. Besides, the central recirculating flow region shape and size are affected by the momentum ratio and swirl level of the central jet. When the swirl intensities of the two coaxial jets are at their maximum, LDV measurements evidence on the burner axis tangential velocity fluctuations at a frequency of about 86 Hz; a POD-based phase average of the PIV maps allows recognizing the presence of a Precessing Vortex Core (PVC) which induces a periodic merging of the two jets. Those results can be of significance in the design of double swirl burners and for the control of the combustion process. Nevertheless, further tests are required to extend the current analysis to combustion conditions.

1. Introduction

Swirling flows find application in many engineering fields, examples of applications include gas turbines, liquid rocket engine injectors, burners, cyclone separators, etc. [1,2]. Their technological relevance, along with their richness in phenomena, has triggered many theoretical, experimental, and numerical investigations aiming at unveiling their structure and behavior. Double and multiple coaxially mounted swirlers are applied in advanced gas turbine combustors to enhance air–fuel mixing [3,4], and their flow field characteristics are reported to be more complex than those of a single swirler. For double coaxial-swirlers, several works have analyzed the effects of swirl levels and direction, i.e. counter- and co-rotating, on combustion and on the flow structure, see for example [5–8]. Nevertheless, the double swirl burner analyzed in the current work has a somehow original configuration, and our results aim to offer further insight into the effect of swirl on the flow field generated by double swirl burners.

This work starts from our research activity about the staged combustion concept [9], which is implemented in this work using a co-rotating swirl burner composed of a central premixed swirled

injector and a coaxial swirled air jet. The injector is designed so that mixing and swirl generation occur at the same point and close to the outlet section, this configuration is expected to achieve a uniform air/fuel mixture at the outlet section and, at the same time, prevent flame flashback. Some preliminary results about the isothermal mean flow field, flame stability, pollutant emissions and flame structure have already been reported in previous works [10,11]. Nevertheless, the isothermal flow field structure was not fully characterized in those works; thus, this paper offers a more detailed analysis of the influence of the swirl level of the two coaxial jets on the mean flow field. Besides, it also documents the occurrence of a precessing vortex core and provides an analysis of its structure.

2. Experimental Setup and Data Processing Technique

2.1. The confined double swirling burner

The burner, Figure 1, is composed of three elements: the double swirl generator, the octagonal combustion chamber ($80\,mm$ by side and $290\,mm$ in height), and the hood. To allow Stereo-PIV measurements, four out of the eight chamber walls are 5 mm thick transparent quartz windows. The burner is composed of a central injector and a coaxial annular passage, and swirl is imparted to the two streams via axial plus tangential entry swirl generators. The swirl direction is the same for the two jets (i.e., they are co-rotating), and their swirl levels can be controlled independently of one another by separately adjusting their axial and tangential air flows. The central injector is also called the premixed injector because it was designed to premix air and fuel (either methane or hydrogen) [11], while pure air flows in the annular passage.

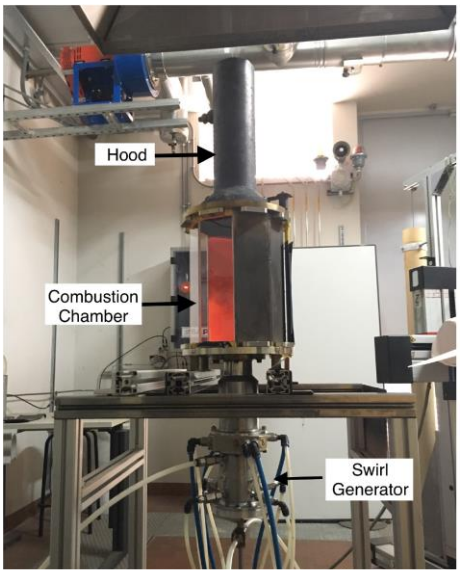

Figure 1: The combustion chamber along with the swirl generator.

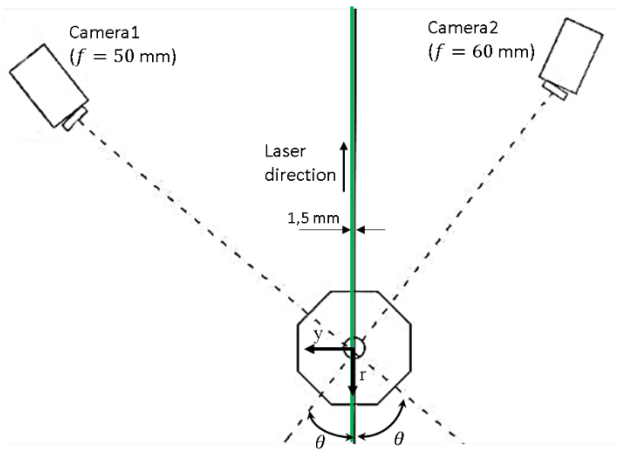

Figure 2: Top view of the Stereo-PIV configuration.

The geometry of the double-swirl generator, that of the swirled premixed injector, and the adopted cartesian reference system x-y-r are shown in Figure 3(a)-(b)-(c), where the y axis is orthogonal to the r-x plane. The instantaneous velocity components along x, y and r are U, W and V, respectively, while the fluctuating velocity components are indicated by u, w and v.

The double swirl generator has a bottle-shaped structure with an internal gas gun, Figure 3(a). The annular jet exhaust in the combustion chamber through a cylindrical nozzle of $L = 40\,mm$ in length, and $D = 36\,mm$ in diameter, Figure 3. The nozzle exit is located $7\,mm$ above a $250\,mm$ diameter circular end plate, named flange in Figure 3(a), and the blockage ratio of the annular jet is $B = D_{p,ext}^2/D^2 \cong 0.44$, where $D_{p,ext} = 24\,mm$ is the external diameter of the central injector. The geometric configuration of the swirl generator for the annular jet is the same as that used in previous

works [12–14] and more detail can be found in [12].

The gas gun is composed of two coaxial pipes, the double pipe gas gun of Figure 3(a), terminating in the swirled premixed injector shown in Figure 3(b). The injector is composed of a cylinder with an external diameter $D_{p,ext}$ and an internal diameter $D_{p,int} = 20\ mm$, while the coaxial central head has a diameter $D_{j,p} = 11\ mm$, see Figure 3(b)-(c). The cylinder is mounted flush with the burner nozzle, while the central head is located $11.5\ mm$ below the exit section of the cylinder, Figure 3(b). The central pipe delivers the air to the central head; the latter injects the air flow in the tangential direction through twenty holes, each having a diameter $d_{tg,p} = 2\ mm$, Figure 3(b). The fuel flows through the $1\ mm$ wide annular gap between the two coaxial pipes and is injected in the axial direction. For safety reasons, since the work is focused on the isothermal flow field, the fuel is replaced by air, and the air flow rate is set to have the same momentum as a methane flow corresponding to a thermal power of 16 kW. All tests are performed by keeping both the total and premix air flow rates constant; which would correspond to operating at a constant global equivalence ratio and constant thermal power under combustion conditions; thus, the swirl level of the primary jet and the momentum ratio cannot be set independently, and increasing the former reduces the latter.

All flow rates are measured and controlled independently one from another by four thermal mass flow meters and controllers, the estimated error on the measured flow rates is about ±1% of reading.

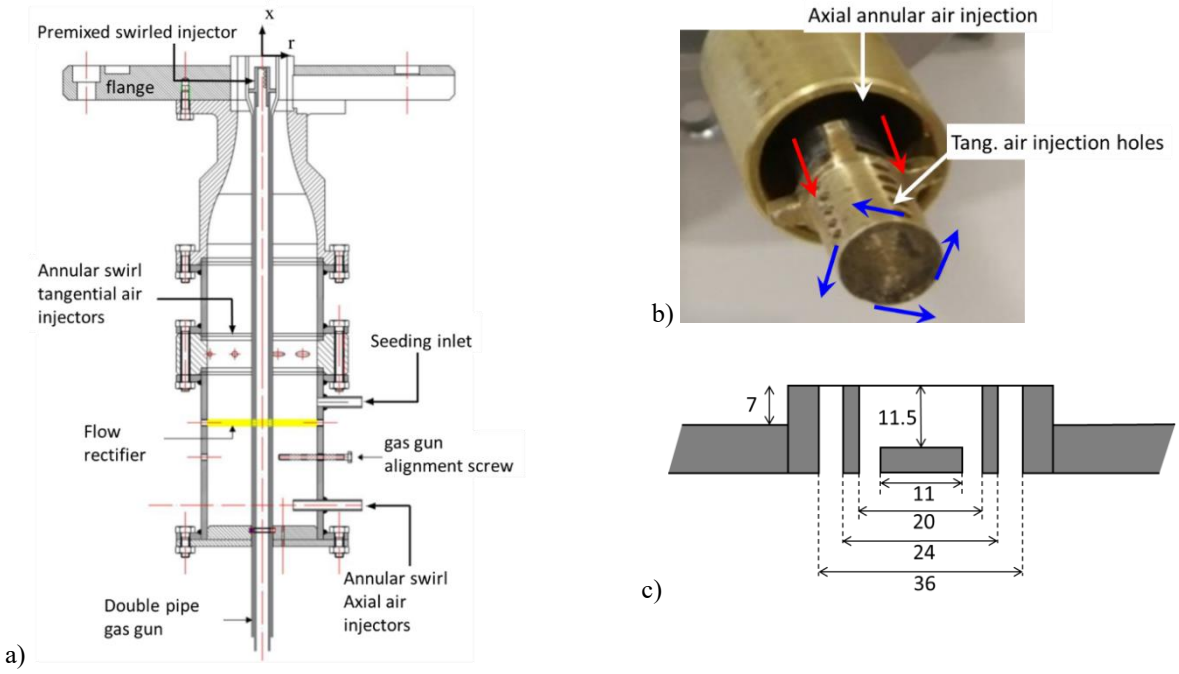

Figure 3: (a) Section of the double swirl generator, (b) detail of the premixed injector with the central head pulled out of the cylinder to make it visible, (c) detail of the nozzle exit section (not in scale).

2.2. Stereo PIV technique

The stereoscopic PIV used to characterize the flow field is composed of two CCD cameras having a resolution of 1344x1024 pixels and equipped with interferential band pass filters ($10\ nm$ FWHM bandpass, $532\ nm$ center wavelength) and Scheimpflug adapters. A $50\ mm$ focal length lens is used for camera 1, while a $60\ mm$ focal length lens is used for camera 2, the aperture of both lenses is set to $F\# = 8$. The two cameras view the laser sheet from opposite sides, both at an angle of about 45°, and oriented in the particle's forward scattering direction so as to maximize the particle image luminosity, Figure 2. The width of the quartz windows reduces the horizontal field of view of the camera to about $3.8D$, while the vertical field of view is limited by the size of the CCD to about $2.9D$.

A $532\,nm$ wavelength laser beam is generated by a dual cavity Nd-Yag laser and shaped into a light sheet about $1.5\,mm$ thick. The light sheet is vertically oriented and crosses the combustion chamber along a nozzle diameter; this allows to record the flow structure evolution in the axial direction. The inner sides of the lateral metallic walls and of the flange are covered by an orange fluorescent paint, partially visible in Figure 1(a), in this way the intensity of the reflected laser light picked up by the camera is reduced because the fluorescent emission of the paint is filtered out by the interferential filter.

Both the annular jet and the central jet are seeded by oil droplets ($\rho_{oil} = 880\ kg/m^3$ at $20\,°C$) with a mean diameter of $d_p \cong$ 1-2 μm, and generated by two separate jet atomizers. For good tracking, the Stokes number $S_t = \tau_p\ /\tau_u$, defined as the ratio between the characteristic time of the oil droplet τ_p and the characteristic time of the flow field τ_u, must be much smaller than 1. In our case $\tau_p = \frac{\rho_{oil} d_p^2}{\mu_{air}} = 2.7\ \mu s$, where μ_{air} is the dynamic viscosity of the air; while for a swirling flow we estimated $\tau_u = \frac{r_{Wmax}}{W_{max}} = 1\ ms$, where W_{max} is the maximum tangential velocity and r_{Wmax} is the radial position of W_{max}. Thus, the Stokes number is $S_t = 0.0024$ and the tracer fidelity condition can be considered satisfied.

Dantec's DynamicStudio software is used to acquire and process the images. Stereo PIV operates in double frame mode, and the time between pulses is set in the range of 15-25 μs, depending on the swirl intensity. For each flow condition, 750 pairs of images were acquired by each camera at a frequency of $4.5\,Hz$. To remove the background luminosity from the PIV images, the mean of 20 images, taken without any flow and any tracers, is subtracted to each PIV image. The images are then dewarped using the pinhole model to obtain a constant and isotropic spatial resolution, finally an image balancing filter, with a smooth cell size of 7 by 7 pixels, is applied to correct for the non-uniformities of the laser light sheet.

An iterative multi-grid, multi-pass, cross-correlation-based algorithm with a final interrogation area of 16 by 32 pixels (vertical x horizontal) with a 50% overlap in both directions is implemented, while vector validation is enforced through both peak validation and the universal outlier detection algorithms [15]. Finally, the moving average filter, based on a 3 by 3 neighborhood size, is applied to the velocity maps. The resolution of the PIV map, based on the interrogation area size, is about $0.038D$ by 0.076D along r and x, respectively. The rectangular shape and the size of the interrogation area is a tradeoff between the resolution along r, where the steeper velocity gradients are expected, and the signal to noise ratio in the cross-correlation. Eventually, the third velocity component is reconstructed from the pair of 2D vector fields. Errors in the alignment between the laser sheet and calibration target are minimized using the disparity vector map derived from the PIV images.

By assuming a 95% confidence interval, the relative statistical error of the mean velocity results to be $\varepsilon_{velocity} = \frac{1.96}{U_{bulk}} * \sqrt{\frac{mean(\overline{v'^2})}{N}} = \pm$ 2%, where N is the sample size of independent samples, $U_{bulk} \cong 7.74\ m/s$ is the bulk axial velocity, and $mean(\overline{v'^2}) \cong 2$ m/s is the spatial mean value of the r.m.s. velocity fluctuations. The 750 Stereo PIV maps are considered statistically independent, since the PIV sampling time, $T_{SPIV} = \frac{1}{4.5\text{Hz}} \cong 0.22$ s, is much larger than the double of the integral time scale $T_i = \frac{D}{U_{bulk}} \cong 0.005\ s$, [16].

2.3. Flow parameters

Swirling jets are commonly characterized by a non-dimensional swirl number, S; for unconfined incompressible flow, assuming both the boundary-layer approximations and negligibly small turbulent stresses, the swirl number is given by equation (1), where R is the nozzle radius [17].

$$S = \frac{\int_0^R r^2(UW)dr}{R\int_0^R r\left(U^2 - \frac{1}{2}W^2\right)dr} \tag{1}$$

In our case two different swirl numbers need to be evaluated, one for each swirled jet. For an axial plus tangential swirl generator, an easier way to monitor the swirl number is by using the geometric swirl number (S_g) as proposed in [18,19]; thus, the geometric swirl numbers for the central jet, $S_{g,p}$, and the annular jet, $S_{g,s}$, are defined by equations (2) and (3), respectively.

$$S_{g,p} = \frac{D_{j,p} D_{p,int}}{10 * d_{tg,p}^2} \left(SR_p\right)^2 \tag{2}$$

$$S_{g,s} = \frac{\pi R_o D}{2A_{T,s}} (SR_s)^2 \tag{3}$$

where $R_o = 40\ mm$, $A_{T,s}$ is the total area of the tangential holes in the outer swirler, and SR_p and SR_s are the split ratios of the central and outer jets, respectively. The split ratios defined by equations (4) represent the fraction of the mass flow rate injected tangentially, and $\dot{m}_{tg,p}$, $\dot{m}_{ax,p}$, $\dot{m}_{tg,s}$ and $\dot{m}_{ax,s}$ are the tangential and axial mass flow rates of the central jet and the tangential and axial mass flow rates of the annular jet, respectively.

$$SR_p = \frac{\dot{m}_{tg,p}}{(\dot{m}_{ax,p} + \dot{m}_{tg,p})} \qquad SR_s = \frac{\dot{m}_{tg,s}}{(\dot{m}_{ax,s} + \dot{m}_{tg,s})} \tag{4}$$

The Reynolds number is defined as $Re = U_{bulk} D \,/\, \nu$, where $D = 36\ mm$ is the nozzle diameter, ν is the kinematic air viscosity, and $U_{bulk} = 4\left(\dot{m}_{ax,p} + \dot{m}_{tg,p} + \dot{m}_{tg,s} + \dot{m}_{ax,s}\right)/(\pi \rho D^2)$ is the bulk axial velocity. In the present work, the total mass flow is kept constant, corresponding to a fixed Reynolds number of about 19500.

The near-field development of turbulent coaxial jets is known to be governed by the ratio of the annular to the central jet momentum flux, i.e. the momentum flux ratio MR, defined by equation (5) [20,21], where B is the blockage ratio defined in section 2.1. Being the swirl level of the central jet varied by varying $\dot{m}_{tg,p}$, and because $\dot{m}_{ax,p}$ is kept constant (corresponding to a fixed fuel flow rate), the mass flow rate of the annular jet must be changed accordingly to keep the total flow rate constant. This implies that the momentum flux ratio decreases as $S_{g,p}$ increase.

$$MR = \left[\left(\frac{\dot{m}_{tg,s} + \dot{m}_{ax,s}}{\dot{m}_{ax,p} + \dot{m}_{tg,p}}\right)\left(\frac{D_{s,int}^2 / D^2}{1 - B^2}\right)\right]^2 \tag{5}$$

The experimental conditions analyzed in the present work, along with the values of the corresponding nondimensional parameters, are shown in Table 1.

Table 1 Experimental conditions

Test n	$\dot{m}_{ax,p}$ g/s	$\dot{m}_{tg,p}$ g/s	$\dot{m}_{ax,s}$ g/s	$\dot{m}_{tg,s}$ g/s	SR_p –	SR_s –	$S_{g,p}$	$S_{g,s}$	MR
4A	0.43	2.72	4.47	1.91	0.864	0.30	4.11	2.6	1.3
5A	0.43	1.09	5.61	2.41	0.719	0.30	2.84	2.6	8.6
6A	0.43	0.00	6.38	2.72	0.000	0.30	0.00	2.6	140
10A	0.43	2.72	3.19	3.19	0.864	0.50	4.11	7.2	1.3
11A	0.43	1.09	4.01	4.01	0.719	0.50	2.84	7.2	8.6
12A	0.43	0.00	4.56	4.56	0.000	0.50	0.00	7.2	140

2.4. Phase Average based on POD

The triple velocity decomposition scheme, introduced by Hussain and Reynolds [22], is applied to our velocity measurements to highlight the periodic fluctuations contained in the flow field. Thus, the instantaneous velocity vector field is decomposed as the sum of a time mean part, $\vec{\bar{c}}(\vec{x})$, a randomly fluctuating velocity field $\overrightarrow{c'}(\vec{x}, t)$, and a coherent fluctuating field, $\vec{\tilde{c}}(\vec{x}, t)$. The phase average method extracts the coherent part $\vec{\tilde{c}}(\vec{x}) = \vec{\bar{c}}(\vec{x}) + \vec{\tilde{c}}(\vec{x}, t)$ by conditionally averaging the instantaneous velocity fields according to the phase of oscillation, $\theta(t)$, of the coherent fluctuation. The phase $\theta(t)$ can be

extracted from an external reference signal locked to the velocity fluctuation [23] or computed off-line using a velocity time series extracted from the same time resolved velocity maps to phase average [24]. In the present case the Stereo PIV operates at a frequency too low to time-resolve the coherent structure, and an external reference signal is not available; thus, the phase angle is obtained using the POD method as done in [14]. The POD method decomposes the fluctuating part of the velocity field as a linear combination of the temporal coefficients $a_j(t)$, and spatial modes $\vec{\Psi}_j(\vec{x})$, as per equation (6).

$$\vec{\hat{c}}(\vec{x},t) + \vec{c'}(\vec{x},t) = \sum_{j=1}^{N} a_j(t)\vec{\Psi}_j(\vec{x}) \quad (6)$$

The POD method was originally introduced in fluid mechanics by Lumley [25] to extract coherent structures in turbulent flows. It is extensively treated in various papers and books, and further information can be found for example in [26,27]. In the present work, POD is implemented according to the method of snapshots proposed by Sirovich [28].

The phase angle $\theta(\mathrm{j})$ is computed from the time coefficients $a_1(j)$ and $a_2(j)$ of the first two most energetic POD modes [14,29–31] as per equation (7), where j is the $j-th$ instantaneous velocity map, and λ_1 and λ_2 are the eigenvalues of POD modes 1 and 2, respectively.

$$\theta(j) = \arctan\left(\frac{\sqrt{2\lambda_1}}{a_1(j)}\frac{a_2(j)}{\sqrt{2\lambda_2}}\right) \quad (7)$$

The velocity maps are sorted according to their phase angles $\theta(j)$ and grouped in phase slots of width $\Delta\theta$. Eventually, maps belonging to the same phase slot are averaged together. The phase slots are arranged to partially overlap; in this way the number of phase slots increases and their angular distance decreases, giving a smoother $3D$ reconstruction of the coherent velocity field [14], while the slot width $\Delta\theta$, i.e. the phase resolution, stay constant. As a tradeoff between angular resolution and statistical convergence, we set $\Delta\theta = \pi/6$ radians, i.e. 30°, and the angular distance between slots to $\pi/12$ radians, i.e. 15°, so to have on average about 62 instantaneous maps in each phase bin and 24 phase averaged maps.

3. Experimental Results

3.1. Mean flow morphology

The mean flow structure is described by nondimensional mean axial velocity maps, $\bar{U}/U_{bulk}$, where the spatial coordinates have been normalized by the burner nozzle diameter D. The velocity maps also show the streamlines (black lines), i.e. lines tangent to the projection of velocity vectors in the measurement plane, along with the iso-line of zero-axial velocity (while lines) to highlight the reverse flow regions, Figure 4(a)-(f).

All the analyzed cases show an outer recirculating zone (ORZ) located between the chamber wall and the swirled jet, which originates from the combination of jet entrainment and chamber wall confinement. At $S_{g,s} = 7.2$ the position of the ORZ is slightly affected by the value of $S_{g,p}$ and varies between $x/D \cong 1.4$ and $x/D \cong 1.6$, Figure 4(b)-(d)-(f). At $S_{g,s} = 2.6$ and at the two lowest primary swirl levels, i.e. $S_{g,p} = 0$ and $S_{g,p} = 2.84$, two outer recirculation regions develop, Figure 4(a)-(c), while at the highest primary swirl levels, i.e. $S_{g,p} = 4.11$, only the upper ORZ is visible, Figure 4(e). The shape of the two ORZ slightly changes by changing the value of $S_{g,p}$, and the position of the upper ORZ moves between $x/D \cong 2$ and $x/D \cong 2.4$ by changing $S_{g,p}$.

The differences in the outer recirculation zone observed between $S_{g,s} = 2.6$ and $S_{g,s} = 7.2$, could be a manifestation of a stronger jet entrainment originated by a higher outer swirl level $S_{g,s}$; i.e. at $S_{g,s} = 7.2$ the stronger entrainment makes the ORZ to reside further upstream respect to the case $S_{g,s} = 2.6$. Incidentally, for an unconfined swirling jet Cozzi et al. have shown that the jet entrainment increases by increasing the swirl level [13].

At $S_{g,s} = 2.6$, both the swirl level and the momentum ratio of the central jet have a profound impact on the flow structure, they control the appearance and the location of the vortex breakdown

phenomena, along with the shape of the associated reverse flow region. For a primary swirl $S_{g,p} = 0$ and $MR \cong 140$, Figure 4(a), the jet width decreases by moving downstream, showing its minimum width at about $x/D \cong 0.55$; past that point, the jet width increases due to the presence of the central recirculation zone. The latter is asymmetric, extends downstream outside the field of view, and has an upstream stagnation point located at $x/D \cong 0.78$. The central recirculation zone is the manifestation of the vortex breakdown phenomena induced by the adverse pressure gradient originated by the decay of azimuthal velocity downstream. A region of low axial velocity embedding two small reverse flow regions is visible close to the central injector, $x/D \lesssim 0.3$, Figure 4(a). The overall jet structure shows some resemblance with that of an annular swirling jet at low-intermediate swirl level as described in unconfined condition by Vanierschot et al. [32] and in confined condition by Percin et al. [33], so it could be speculated that for this very high value of MR the central injector mainly acts as a bluff body; nevertheless, the swirl level and momentum of the central jet can have a role in defining the detail of the near field flow structure and the axial location of the vortex breakdown. By increasing the swirl level of the central jet, $S_{g,p}$, to 2.84, the reverse flow region disappears, and the axial velocity is directed only downstream in the whole jet region, Figure 4(c). By further increasing $S_{g,p}$ to 4.11 the swirl level of the central jet is strong enough to generate the vortex breakdown along with a reverse flow region, Figure 4(e). Now the reverse flow region has a thin and elongated shape, starts directly at the premixed injector, and ends at approximately $x/D = 1.6$, Figure 4(e).

As described in section 2.3. and shown in Table 1, the three different primary swirl levels correspond to quite different momentum ratios, thus the above behaviors are likely due to the combined effect of $S_{g,p}$ and MR.

At $S_{g,s} = 7.2$, and independently from the primary swirl level $S_{g,p}$, both the vortex breakdown and the associated recirculating flow region are present, while along the burner centerline the axial velocity is always direct toward the nozzle. The shape and size of the reverse flow region are controlled by the swirl level and momentum ratio of the central jet, Figure 4(b)-(d)-(f). At $S_{g,p} = 0$ and $MR \cong 140$ the recirculating flow appears as an axisymmetric toroidal vortex, and the minimum axial velocity, $\overline{U}/U_{bulk} \cong -0.67$, occurs on the burner axis at $x/D \cong 0.7$, Figure 4(b). By increasing the primary swirl to $S_{g,p} = 2.84$, the reverse flow loses its axial symmetry, the minimum axial velocity reduces to $\overline{U}/U_{bulk} \cong -0.38$ and its location moves downstream at $x/D \cong 1.0$. In our test, a higher primary swirl corresponds to a lower momentum ratio; thus, the higher momentum of the central jet counteracts the reverse flow slowing it down. For the same reason, the width of the reverse flow shrinks close to the nozzle exit as compared to the case $S_{g,p} = 0$; moreover, the higher swirl level of the inner jet promotes a wider radial reverse flow between $0.4 \leq x/D \leq 1.6$, compare Figure 4(b) and Figure 4(d).

By further increasing $S_{g,p}$ to 4.11, the reverse flow region becomes more asymmetric and takes the shape of an inverted cone, now the vortex breakdown is triggered by the high swirl level of the central jet, indeed the strongest reverse flow occurs at the exit plane of the central injector and likely extends inside the injector itself (not visible); with respect to the case $S_{g,p} = 2.84$ the maximum reverse axial velocity increases to $\overline{U}/U_{bulk} \cong -0.67$, equaling the value measured for the case $S_{g,p} = 0$, but now such maximum occurs at the injector exit, Figure 4(f). With respect to the case $S_{g,s} = 2.6$ and $S_{g,p} = 4.11$, the stronger swirl level of the annular stream makes the reverse flow to extend beyond the field of view and to increase in width downstream, compare Figure 4(f) and Figure 4(e).

The above results evidence the mean flow structure to be significantly altered by the different swirl levels and momentum ratio, and different flame structures can be expected under combustion conditions.

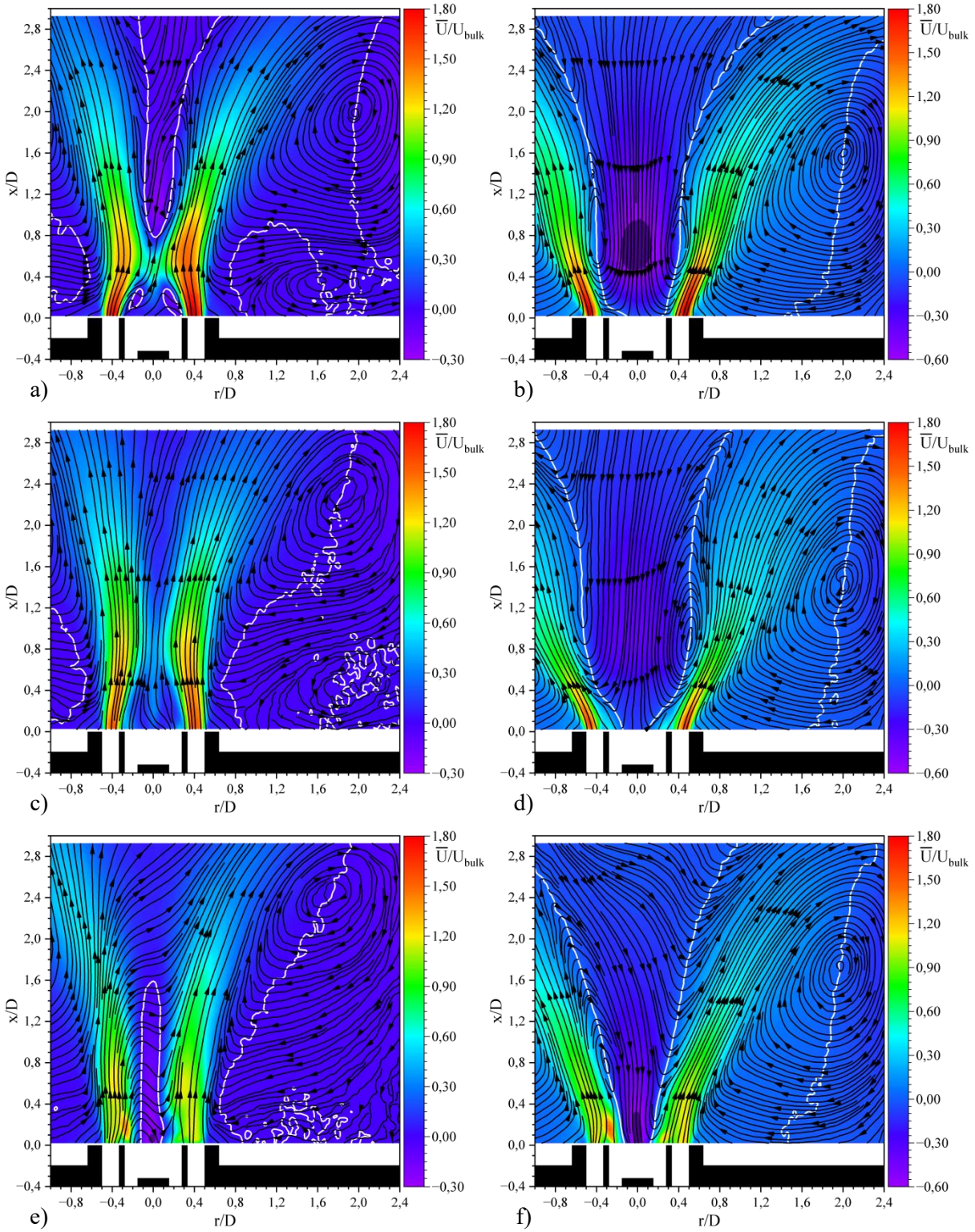

Figure 4: Streamlines and contours plots of the mean axial velocity, $\overline{U}/U_{bulk}$ in the longitudinal plane. $S_{g,s} =$ 2.6 and (a) $S_{g,p} = 0$, $MR \cong 140$; (c) $S_{g,p}$ =2.84, $MR \cong 8.6$; (e), $S_{g,p}$ =4.11, $MR \cong 1.3$. $S_{g,s} =$ 7.2 and (b) $S_{g,p} = 0$, $MR \cong 140$; (d) $S_{g,p}$ =2.84, $MR \cong 8.6$; (f), $S_{g,p}$ =4.11, $MR \cong 1.3$. The white solid line is the iso-line $\overline{U}/U_{bulk} = 0$.

3.2. Phase-averaged results

For the test case 10A (see Table 1), preliminary velocity measurements by LDV on the burner axis and close to the nozzle exit, i.e. at $r/D = 0$ and $x/D \cong 0.08$, evidenced strong tangential velocity fluctuation having a frequency, f, of about 86 Hz, Figure 5(a). The POD analysis of the instantaneous stereo PIV maps reveals that the first two POD modes have a similar and much higher energy level than the other modes, Figure 5(b); besides, they show similar spatial patterns, spatially shifted one respect to the other of about $1/4$ wavelength (i.e. $\pi/2$), Figure 6; all those features are indicative of a coherent flow structure.

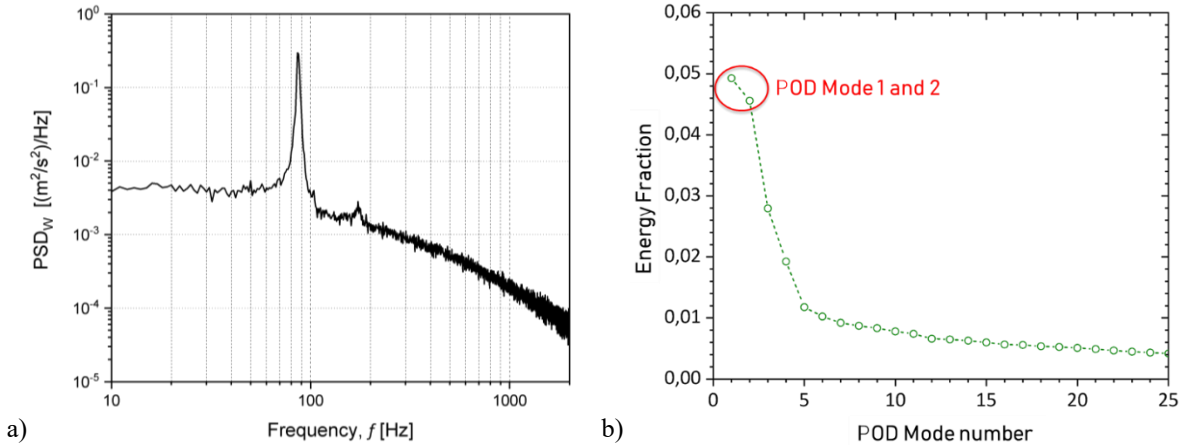

a) b)

Figure 5: Power spectral density of the tangential velocity at ($r/D = 0$, $x/D \cong 0.08$). Swirl levels: $S_{g,p} =$ 4.11 and $S_{g,s} =$ 7.2 (test case 10A in Table 1).

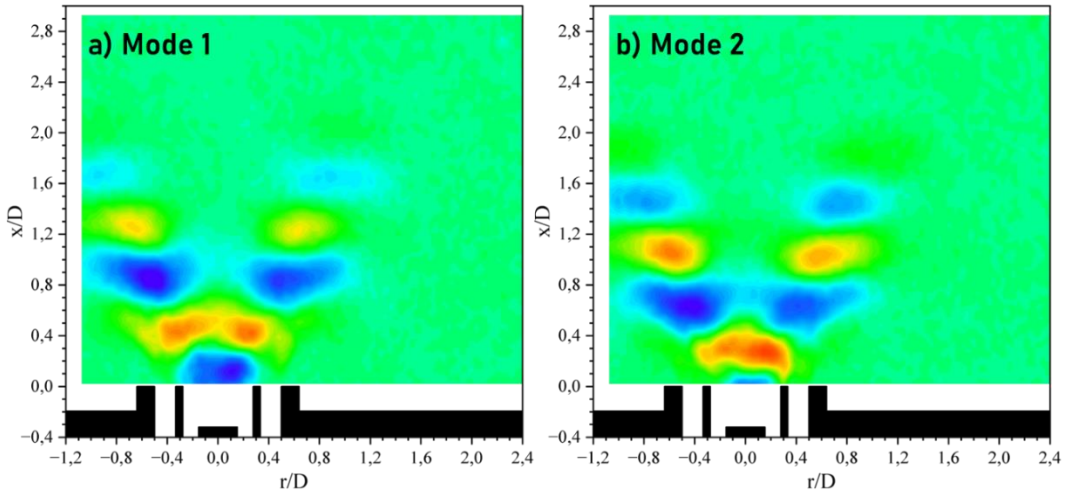

Figure 6: Contour of the radial velocity component, V_{POD}, of the first two POD modes, (a) mode 1 (b) mode 2. Test case 10A (Table 1), $S_{g,p} =$ 4.11 and $S_{g,s} =$ 7.2.

The phase average method described in section 2.4. is applied to the instantaneous velocity maps to extract the coherent flow field. The phase portrait of the normalized time coefficients $a_1(j)$ and $a_2(j)$, Figure 7, appears rather scattered due to the relatively small energy fraction of the two modes (about 5% each), nevertheless the typical circular distribution, commonly observed for quasi-periodic flows [29], is still recognizable. Legrand et al. state that the phase information can be retrieved in a sufficiently reliable way, when the sum of the energy of the first two POD modes is at least about 10% of the total energy [34]. Nevertheless, for a low swirl jet, they also assume a reliable phase reconstruction when the cumulative energy level of the two modes is just about 8% [34]. In our case, the combined energy of the two modes is 9.5%, very close to Legrand's threshold; besides, if the phase were completely corrupted by noise, the phase average would return something very close to the mean flow field, which is not our case.

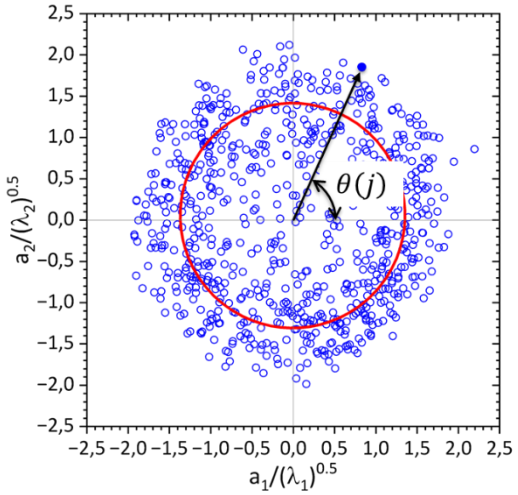

Figure 7: Test case 10A (Table 1), $S_{g,p}$ = 4.11 and $S_{g,s}$ = 7.2. Phase plot of the normalized time coefficients $a_1(j)$ and $a_2(j)$ of the first two POD modes along with the best circle fit of the data (red solid line).

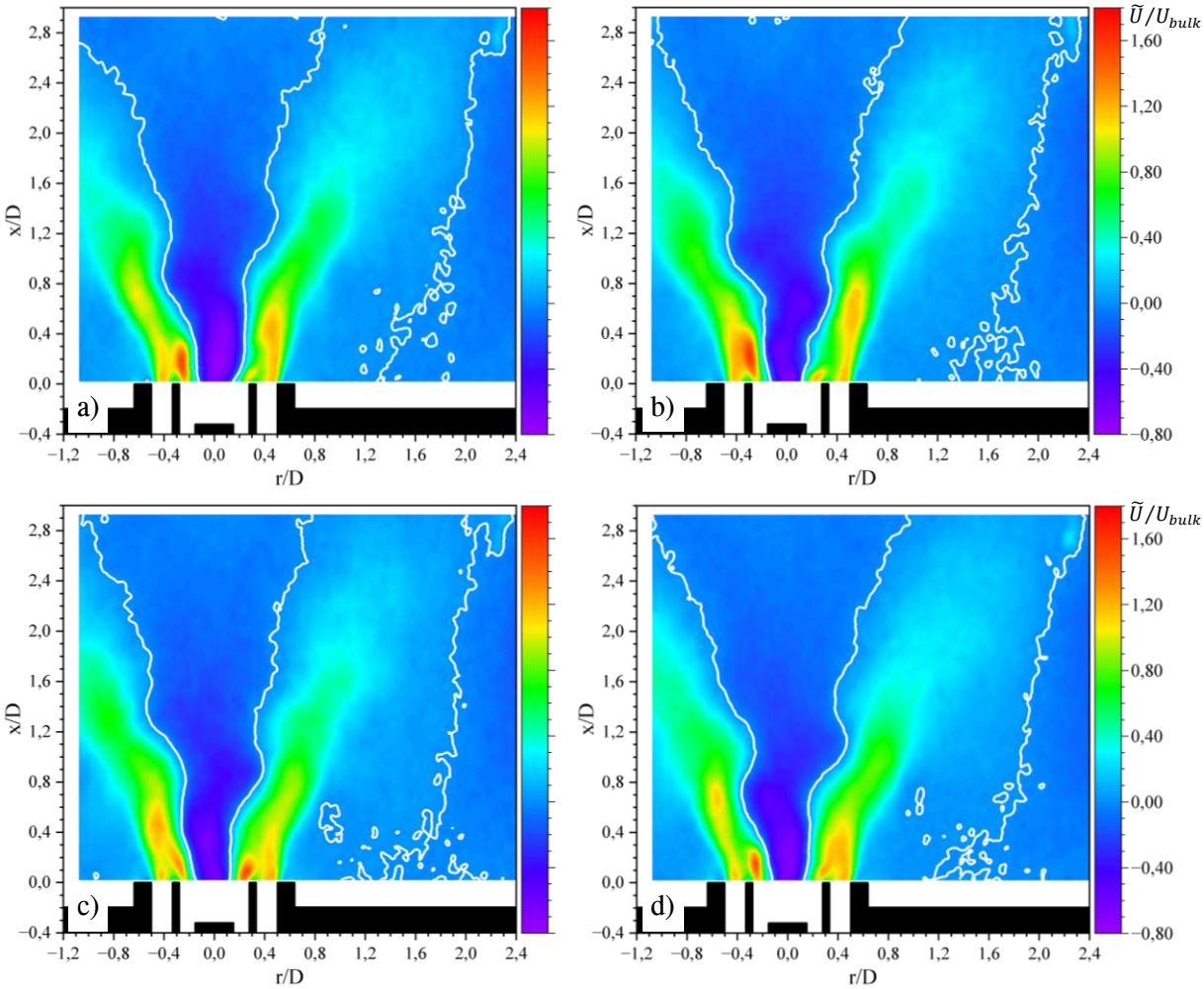

Figure 8: Test case 10A, $S_{g,p}$ = 4.11 and $S_{g,s}$ = 7.2. Non dimensional phase averaged axial velocity $\tilde{U}/U_{bulk}$, solid white line is the isoline of zero axial velocity, while the contour plot is axial velocity. a) $\theta = 0°, b)\ \theta = 90°$, c) $\theta = 180°$, d) $\theta = 270°$

Only the nondimensional phase averaged axial velocity contours, $\tilde{U}/U_{bulk}$, at $\theta = 0°, 90°, 180°$, and $270°$ are reported here. The contours clearly show asymmetry with respect to the geometrical axis, Figure 8(a)-(d); close to the burner exit, $x/D \lesssim 0.3$, two separate axial streams, corresponding to

the central and annular jets, are clearly distinguishable, the highest axial velocity regions move from the left side to the right side of the burner axis when the phase increases from 0° to 180°, compare Figure 8(a) and Figure 8(c), and vice versa from 180° to 360°. In the region below $x/D \cong 0.4$, the outer and central jets attract each other merging into a high axial velocity pocket; this process takes place periodically and appears on the left side of the burner axis when $\theta \lesssim 180°$ and on the opposite side when $\theta \gtrsim 180°$. The periodic merging of the two jets, while not guaranteed to exist also in combustion conditions, could affect mixing and flame stability under combustion conditions; to the authors' knowledge such phenomena has not been reported before in the literature. Downstream of the merging zone, i.e. $x/D \gtrsim 0.4$, the central and outer jets are no longer distinguishable, and a single pocket of highest axial velocity occurs alternately on the right and left side of the burner axis.

Evidence of the vortex breakdown is given by the reverse flow region extending downstream beyond the field of view and bounded in Figure 8 (a)–(d) by two thick white lines. The reverse flow region has a wavy shape, and its boundaries move back and forth in the horizontal direction.

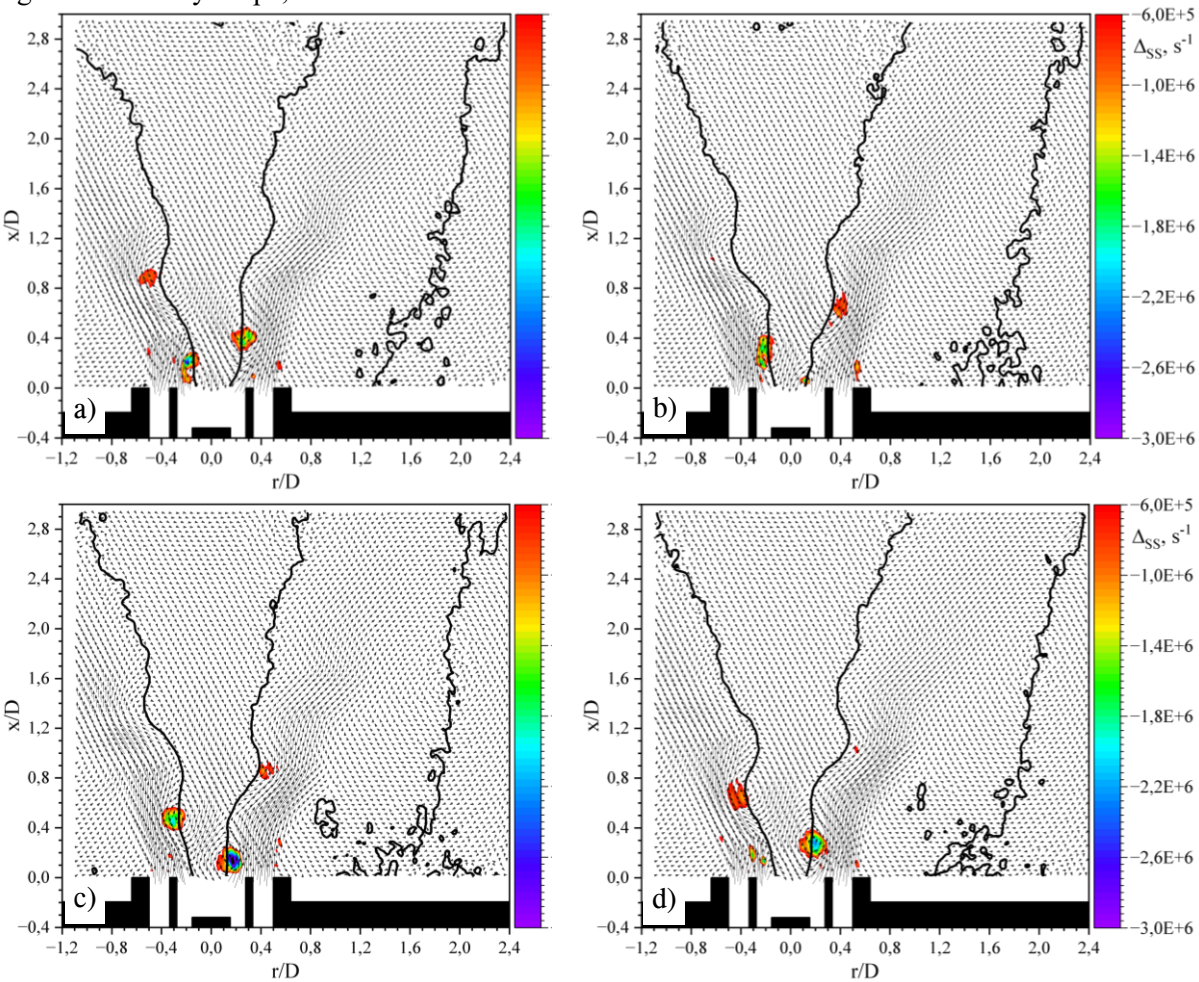

Figure 9: Test case 10A, $S_{g,p}$ = 4.11 and $S_{g,s}$ = 7.2. Swirling strength (contours) superimposed on the in-plane phase averaged velocity (vectors) and isoline of zero axial velocity (solid black lines). a) $\theta = 0°, b)\ \theta = 90°,$ c) $\theta = 180°,$ d) $\theta = 270°$

To shed light on the flow structure, the vortex identification analysis based on the swirling strength criterion is carried out on the phase averaged flow field. This criterion is based on the critical-point analysis of the velocity gradient tensor, and it uses the imaginary part, λ_{ci}, of the complex eigenvalues of the velocity gradient tensor to visualize vortical structures. The quantity λ_{ci} is called the local swirling strength of the vortex, $\lambda_{ci} = 0$ in pure shear flow and $\lambda_{ci} > 0$ in eddies [35]. In Cartesian coordinates and for planar velocity measurements, the condition for complex eigenvalues reduces to

the condition that the discriminant of the characteristic equation of the tensor, Δ_{SS}, given by equation (8), to be negative; thus, vortex locations are identified by regions where $\Delta_{SS} < 0$, with a small abuse in terminology, we will refer to Δ_{SS} as the swirling strength.

$$\Delta_{ss} = \frac{1}{4}\left(\frac{\partial \mathrm{V}}{\partial \mathrm{r}}\right)^2 + \frac{1}{4}\left(\frac{\partial \mathrm{U}}{\partial \mathrm{x}}\right)^2 - \frac{1}{2}\left(\frac{\partial \mathrm{V}}{\partial \mathrm{r}}\right)\left(\frac{\partial \mathrm{U}}{\partial \mathrm{x}}\right) + \left(\frac{\partial \mathrm{U}}{\partial \mathrm{r}}\right)\left(\frac{\partial \mathrm{V}}{\partial \mathrm{x}}\right) \quad (8)$$

The results of the vortex identification analysis, superimposed on the phase averaged in plane velocities, are shown in Figure 9(a)-(d), they reveal concentrated vortices that originate from the central swirled jet and located in the shear layer between the central jet and the reverse flow. The vortices are arranged in a staggered pattern, giving the reverse flow region the observed wavy structure. Besides, vortices on the opposite sides of the reverse flow show opposite vorticity (not shown here), and they appear to move downstream as the phase angle increases. All those features are a clear indication that those vortices are the cross-sectional view, through the measurement plane, of a single helical vortex wrapped around the reverse flow, and such a helical vortex is the manifestation of the precessing vortex core (PVC). Besides, the sign of the tangential velocity (negative on $r/D > 0$ and positive $r/D < 0$) along with the downstream movement of the vortical structure, allows one to state that the helical structure winds in the opposite direction respect to the swirl direction.

The wavy structure of the reverse flow and its left-right wandering observed previously are clearly the manifestation of the interaction between the helical vortex and the reverse flow region.

The periodic merging between the inner and annular jets and the PVC phenomenon appear to be synchronized and connected to each other; indeed, the merging occurs very close to the position of the helical vortex; compare Figure 8 and Figure 9.

The PVC phenomenon is commonly encountered in high swirl flow in both laminar and turbulent flow conditions, and it has been observed in the same burner used here, but without the central injector, at $S = 1.4$ and $Re \cong 21800$, by Cozzi et al. [14]. Anyhow, there are some noticeable differences between the present case and that in [14]: first, the cumulate energy fraction of the first two modes is much smaller than that observed in [14], i.e. about 9 % vs. 43 %; second, the PVC observed by Cozzi et al. shows a strong secondary helical vortex located in the outer shear layer of the jet, while a secondary helical vortex cannot be evidenced here; finally, we observe the vortical structure to fade out downstream $x/D \cong 0.8$, while in [14] it occurs downstream $x/D \cong 1.5$. It is somehow interesting to observe that the ratio $1.5/0.8$ is very close to the ratio of the nozzle diameter of [14] and that of our primary jet, i.e. $36\ mm/20\ mm$. The differences between our results and those of Cozzi et al. can be attributed to the different configurations (single vs. double swirl, unconfined vs. confined) and to the different operating conditions, nevertheless it is worth noting that for our double swirl configuration, a secondary helical vortex cannot be detected in the PVC structure.

4. Conclusions

This paper analyzes the isothermal flow field structure of a double coaxial swirl burner, composed of a central swirled injector and an annular swirled stream. Under isothermal conditions, the fuel is replaced with air for safety reasons, and the air flow rate is set as to have the same momentum of a methane flow rate of $16\ kW$. The influence of the outer and inner swirl levels on the isothermal field was characterized at a fixed Reynolds number, $Re = 19500$, using the Stereo-PIV technique; two different secondary swirl levels, $S_{g,s}$, and three different primary swirl levels. $S_{g,p}$, have been investigated. All tests were performed by keeping both the total air flow rate and the axial air flow rate in the central injector constant; thus, by increasing the swirl level of the primary jet, the momentum ratio decreases.

At the lowest secondary swirl level, $S_{g,s} = 2.66$, significant changes in the time mean flow structure are observed as the swirl level of the central jet $S_{g,p}$ is increased from its minimum to its maximum value. At $S_{g,p} = 0$ an asymmetric reverse flow region, originated by the vortex breakdown phenomenon, is observed downstream $x/D \cong 0.5$, while two small reverse flow regions are observed upstream. By increasing $S_{g,p}$ to 2.84, the reverse flow regions and the stagnation points in the jet

disappear completely; indeed, the mean axial velocity points downstream in the whole jet region. By further increasing $S_{g,p}$ to 4.11, the vortex breakdown shows up again, inducing a thin and elongated reverse flow region attached to the central injector.

At $S_{g,s} = 7.2$, the vortex breakdown occurs for all the tested $S_{g,p}$ values. At $S_{g,p} = 0$, the vortex breakdown has an axisymmetric shape, and shows a strong reverse flow region. By increasing $S_{g,p}$ to 2.84, the vortex breakdown loses its axial symmetry, and close to the injector exit, the reverse flow region width shrinks due to the lower MR, while it increases further downstream. By further increasing $S_{g,p}$ to 4.11, the reverse flow takes the shape of an inverted cone, and the maximum reverse flow velocity moves closer to the central injector. At that highest $S_{g,p}$, the frequency spectra of LDV velocity measurements show periodic velocity fluctuations at a frequency of about $86\,Hz$. A POD based phase average of the instantaneous stereo PIV maps, evidences the velocity fluctuation to be associated to a coherent flow structure, the processing vortex core, originated by the central injector. Besides, the PVC induces the two coaxial and co-swirling jets to periodically merge, to authors' knowledge this phenomenon seems not to be documented in the literature.

The experimental results show that changing the swirl level of the two jets, and the momentum ratio, gives rise to very different flow structures, these results can be of significance in designing double swirl burners and for the control of the combustion process. However, further tests are required to extend the results to combustion conditions.

References

[1] Gupta AK, Lilley DG SN 1984 *Swirl flows*
[2] Kang Z, Wang Z guo, Li Q and Cheng P 2018 Review on pressure swirl injector in liquid rocket engine *Acta Astronaut.* **145** 174–98
[3] Liu Y, Sun X, Sethi V, Nalianda D, Li Y-G and Wang L 2017 Review of modern low emissions combustion technologies for aero gas turbine engines *Prog. Aerosp. Sci.* **94** 12–45
[4] Lazik W, Doerr T, Bake S, v. d. Bank R and Rackwitz L 2008 Development of Lean-Burn Low-NOx Combustion Technology at Rolls-Royce Deutschland *Volume 3: Combustion, Fuels and Emissions, Parts A and B* vol 3 (ASMEDC) pp 797–807
[5] Yuasa S 1986 Effects of swirl on the stability of jet diffusion flames *Combust. Flame* **66** 181–92
[6] Merkle K, Haessler H, Büchner H and Zarzalis N 2003 Effect of co- and counter-swirl on the isothermal flow- and mixture-field of an aairblast atomizer nozzle *Int. J. Heat Fluid Flow* **24** 529–37
[7] Degenève A, Mirat C, Caudal J, Vicquelin R and Schuller T 2019 Effects of Swirl on the Stabilization of Non-Premixed Oxygen-Enriched Flames above Coaxial Injectors *J. Eng. Gas Turbines Power* **141**
[8] Degenève A, Vicquelin R, Mirat C, Caudal J and Schuller T 2021 Impact of co- and counter-swirl on flow recirculation and liftoff of non-premixed oxy-flames above coaxial injectors *Proc. Combust. Inst.* **38** 5501–8
[9] Cozzi F and Coghe A 2012 Effect of air staging on a coaxial swirled natural gas flame *Experimental Thermal and Fluid Science* vol 43 pp 32–9
[10] Cozzi F, Francabandiera A and Zampini L 2018 Experimental investigation of the isothermal flow field of a double swirl burner *Work-in-Progress Poster 37th International Symposium on Combustion* (Dublin, Ireland: 37th International Symposium on Combustion)
[11] Cozzi F, Motta F, Cobianchi F, Zampini L and Francabandiera A 2019 Experimental Analysis of a Double Swirl Burner *42nd Meeting of the Italian Section of the Combustion Institute* ed F Scala, E Salzano, M Commodo, A Tregrossi and A Gomez-Barea (Ravenna) pp 1–6
[12] Sharma R and Cozzi F 2017 Experimental Study of Unconfined and Confined Isothermal Swirling Jets *Int. J. Mech. Mechatronics Eng.* **11** 386–96
[13] Cozzi F, Coghe A and Sharma R 2018 Analysis of local entrainment rate in the initial region of

isothermal free swirling jets by Stereo PIV *Exp. Therm. Fluid Sci.* **94** 281–94
[14] Cozzi F, Sharma R and Solero G 2019 Analysis of coherent structures in the near-field region of an isothermal free swirling jet after vortex breakdown *Exp. Therm. Fluid Sci.* **109** 109860
[15] Westerweel J and Scarano F 2005 Universal outlier detection for PIV data *Exp. Fluids* **39** 1096–100
[16] Martinelli F, Olivani A and Coghe A 2007 Experimental analysis of the precessing vortex core in a free swirling jet *Exp. Fluids* **42** 827–39
[17] Vignat G, Durox D and Candel S 2022 The suitability of different swirl number definitions for describing swirl flows: Accurate, common and (over-) simplified formulations *Prog. Energy Combust. Sci.* **89** 100969
[18] Feikema D, Chen RH and Driscoll JF 1990 Enhancement of flame blowout limits by the use of swirl *Combust. Flame* **80** 183–95
[19] Claypole TC and Syred N 1981 The effect of swirl burner aerodynamics on NOx formation *Symp. Combust.* **18** 81–9
[20] Rehab H, Villermaux E and Hopfinger EJ 1998 Geometrical effects on the near-field flow structure of coaxial jets *AIAA J.* **36** 867–9
[21] Rehab H, Villermaux E and Hopfinger EJ 1997 Flow regimes of large-velocity-ratio coaxial jets *J. Fluid Mech.*
[22] Hussain AKMF and Reynolds WC 1970 The mechanics of an organized wave in turbulent shear flow *J. Fluid Mech.* **41** 241–58
[23] Martinelli F, Cozzi F and Coghe A 2012 Phase-locked analysis of velocity fluctuations in a turbulent free swirling jet after vortex breakdown *Exp. Fluids* **53** 437–49
[24] Negri M, Cozzi F and Malavasi S 2011 Self-synchronized phase averaging of PIV measurements in the base region of a rectangular cylinder *Meccanica* **46** 423–35
[25] Lumley JL 1967 The structure of inhomogeneous turbulence *Atmospheric Turbulence and Radio Wave Propagation, edited by A. M. Yaglom and V. I. Tatarski (Nauka, Moscow)* pp 166–178
[26] Berkooz G, Holmes P and Lumley JL 1993 The proper orthogonal decomposition in the analysis of turbulent flows *Annu. Rev. Fluid Mech.* **25** 539–75
[27] Taira K, Brunton SL, Dawson STM, Rowley CW, Colonius T, McKeon BJ, Schmidt OT, Gordeyev S, Theofilis V and Ukeiley LS 2017 Modal analysis of fluid flows: An overview *AIAA J.* **55** 4013–41
[28] Sirovich L 1987 Turbulence and the dynamics of coherent structures. *Q. Appl. Math.* **45** 561–71
[29] Oudheusden BW van, Scarano F, Hinsberg NP van and Watt DW 2005 Phase-resolved characterization of vortex shedding in the near wake of a square-section cylinder at incidence *Exp. Fluids* **39** 86–98
[30] Oberleithner K, Sieber M, Nayeri CN, Paschereit CO, Petz C, Hege H-C, Noack BR and Wygnanski I 2011 Three-dimensional coherent structures in a swirling jet undergoing vortex breakdown: stability analysis and empirical mode construction *J. Fluid Mech.* **679** 383–414
[31] Stöhr M, Boxx I, Carter C and Meier W 2011 Dynamics of lean blowout of a swirl-stabilized flame in a gas turbine model combustor *Proc. Combust. Inst.* **33** 2953–60
[32] Vanierschot M and Van den Bulck E 2008 Influence of swirl on the initial merging zone of a turbulent annular jet *Phys. Fluids* **20** 105104
[33] Percin M, Vanierschot M and Oudheusden BW va. 2017 Analysis of the pressure fields in a swirling annular jet flow *Exp. Fluids* **58** 1–13
[34] Legrand M, Nogueira J, Tachibana S, Lecuona A and Nauri S 2011 Flow temporal reconstruction from non time-resolved data part II: Practical implementation, methodology validation, and applications *Exp. Fluids* **51** 861–70
[35] Adrian RJ, Christensen KT and Liu ZC 2000 Analysis and interpretation of instantaneous turbulent velocity fields *Exp. Fluids* **29** 275–90